

Full length Article

Considerations of potential runaway motion and physical interaction for speed and separation monitoring

Eugene Kim*, Yoji Yamada, Shogo Okamoto, Mikihiro Sennin, Hiroki Kito

Department of Mechanical Systems Engineering, Nagoya University, Furo-Cho, Chikusa-ku, Nagoya, 464-8603, Japan

ARTICLE INFO

Keywords:

Human-robot collaboration
Speed and separation monitoring
Safety-related sensor
3D Human sensing
Unstructured manufacturing

ABSTRACT

In the field of human-robot collaboration (HRC), the speed and separation monitoring (SSM) collaboration have attracted much attention owing to its non-contact safety strategy. 3D sensing applications are currently of interest for industrial automation technology and are considered to be a promising method for maximizing the efficiency of SSM. However, little attention has been given to the runaway space of the robot or the potential contact due to the foreseeable misuse of the operator. In this study, experiments are conducted using a radar system as an example of a 3D safety-related sensor, and battery assembly scenarios are carried out for the comparison. In the experiment, two different orientations of the robot are tested, considering the potential runaway motion of the robot. Also, the maximum permissible speed of the robot is calculated by geometrical transfer energy, which is based on effective mass and the velocity of the manipulator and human injury criteria. From the experimental results, it is evident that it is better to avoid placing the vertical articulated robot in front of the operator from the perspective of minimizing the effect of runaway motion into the safety distance. Finally, the proposed framework of speed limitation is thought to be an effective method to link SSM and power and force limiting safety function.

1. Introduction

Robots have undoubtedly become a critical resource in the manufacturing sector. Repetitive and simple tasks, or tasks that are difficult and dangerous for humans, can be performed efficiently and safely by robots. However, humans have higher productivity than robots in particular tasks, such as connecting wires and cables. For this reason, human-robot collaboration (HRC) plays an important role in bringing productivity and efficiency one step higher [1,2]. In order to realize the demands for HRC, it is necessary to reduce the risk to an acceptable level, which can only be achieved through sufficient risk assessment [3,4]. Here, the speed and separation monitoring (SSM) function can be utilized in the scenario that uses a non-contact policy for securing the safety of humans while allowing a protective separation distance (PSD) between humans and robots [5,6].

There has been discussion and investigation regarding how to take advantage of the SSM function. Szabo et al. applied the SSM prototype, which was one of the earliest forms that utilize laser scanner-type of safety-related sensors [7]. Furthermore, Marvel et al. evaluated the safety and productivity of the SSM functionality, and several studies were undertaken to investigate the influence of the essential parameters

that supplement the PSD function [8–11]. Another approach was taken by Lacevic et al., which expands the SSM function to entire joints of the robot using a danger field algorithm for calculating avoidance motion [12,13]. In addition, Byner et al. maximized the efficiency of SSM by geometrically computing the distance of the robot to the source of danger [14]. A number of studies have investigated the parameters that supplement the PSD, such as basic parameters [15], a psychological approach [16], and the likelihood of intrusion [17].

However, commercialized robots that are designed for collaboration are not generally operated with the SSM function. Some studies have claimed that the reason for this is the absence of a suitable safety-related sensor [18,19]. On the other hand, the recently launched ISO/TS 62,998 standard, which aims to extend and integrate these safety-related sensors, does not limit the detection principle to a specific medium [20]. These recent trends have led to proposals of 3D detection techniques and to feasibility studies of human presence sensing [21–24]. The high-quality data obtained by these 3D sensors is expected to drastically reduce the distance between humans and SSM implemented robots [18]. Moreover, recent advancements in the framework of collision-free HRC has been reported with various concept using 3D sensors such as machine learning techniques and pose

* Corresponding author.

E-mail address: kim.eugene@a.mbox.nagoya-u.ac.jp (E. Kim).

URL: <http://www.mech.nagoya-u.ac.jp/asi/en/> (E. Kim).

<https://doi.org/10.1016/j.rcim.2020.102034>

Received 10 September 2019; Received in revised form 13 July 2020; Accepted 13 July 2020

Available online 22 July 2020

0736-5845/ © 2020 Elsevier Ltd. All rights reserved.

estimation of human [25,26]. In this respect, it is important that supplemental considerations especially related to safety criteria for SSM when introducing 3D sensors are urgently discussed.

The aforementioned SSM criteria can be applied only to situations when the robot is normally activated and has the capability of aborting when necessary [27]. However, possible faults such as an erratic sensor at the joint level may generate erroneous signals which cause an instant runaway state of the robot [28]. In this respect, some studies have attempted to show how much the runaway volume on the robot manipulator should be estimated at an instant in 3D space. Meanwhile, the runaway motion space may differ with the relative orientation of the robot and the operator since the runaway distance is generally represented as an ellipsoid volume. Based on the pioneering work of Yamada, we will discuss whether the runaway distance can be reduced according to the relative orientation of the human and the robot [29].

For the case of using properly designed SSM, no contact can occur except for intentional or misuse by the human because of the nature of the non-contact oriented collaborative system. However, some of the potential intrusion may be conditionally allowed if the estimated risk is acceptable which will make the application more efficient than solely used SSM. In this case, more attention should be given to the severity of the undesired contact, originating from human error or the ergonomic aspect of risk assessment for the human operators. This may be realized by considering transfer energy between the human and the robot which also indispensable from the viewpoint of a probabilistically worst-case scenario. Thus, the approach of estimating the expected transfer energy of potential contact in the dynamic state will be discussed in this study.

1.1. Contributions

This study presents two approaches for investigating marginal considerations for SSM collaborative method with the 3D sensor usage. One approach is to investigate the effect of the sudden acceleration of the robot due to the runaway motion of the robot. Another approach shows the maximum permissible speed of the robot calculated by geometrical transfer energy. First, an experiment was made to compare the SSM implementation when using a radio wave sensor as an example of a 3D sensor and a conventional minimum distance approach when using a 2D laser scanner. In the experiment, human and robot battery assembly tasks were used to demonstrate a realistic HRC scenario, and experiments have conducted by the participants who have been engaged in the production line for more than two years. Then, the obtained relative motions of the robot and the human are used to calculate the effect of a potential runaway motion of robots based on two relative orientations of an operator and a robot: frontal orientation A, and perpendicular orientation B. Based on effective mass and the relative velocity of the manipulator and the operator obtained in the experiment, the speed limitation of the robot method is discussed.

2. Methodology for non-contact policy between humans and robots

The SSM collaborative operation method secures the operator from collision by continuously monitoring the movements of humans and robots. This method calculates the minimum allowable distance between a human and a robot based on the physical relationship using information from a safety-related sensor. At the moment when the operator is encroaching in terms of the PSD, the robot system designed with SSM method initiate a protective stop and safety-related functions such as turning off any hazardous tools [30]. In this section, potential runaway motion in task space (PRAM-t) is introduced based on the dynamic manipulability ellipsoid (DME).

2.1. Protective separation distance

Fig 1 shows a schematic diagram of the PSD. The formula of the PSD

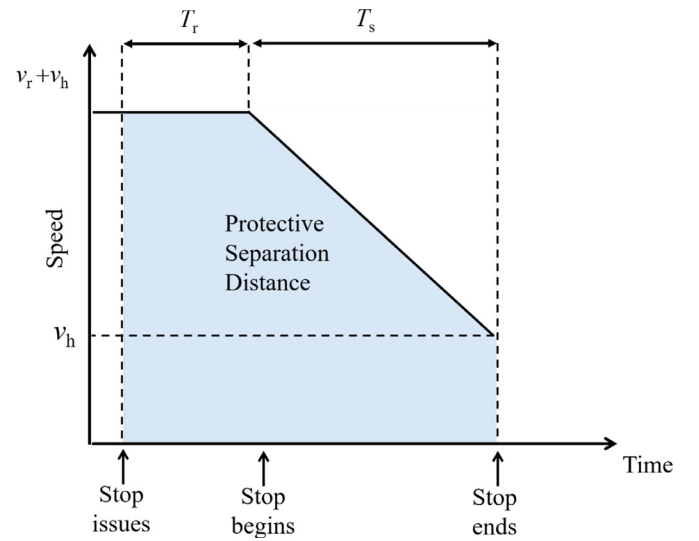


Fig. 1. Illustration of protective separation distance (blue colored area), where v_h and v_r denote the relative speed of the operator and the robot, respectively, defined according to the closest distance plane; T_r denote the global reaction time which includes protective equipment, logical control device, and drive apparatus; and T_s represent the stopping time to make the speed of the robot zero. (For interpretation of the references to colour in this figure legend, the reader is referred to the web version of this article.)

is given by

$$S_p(t_0) = S_h + S_r + S_s + C + Z_d + Z_r. \quad (1)$$

where S_h is the distance that the human can move from the time the stop signal is issued to the robot until the time that the robot is required to stop completely; and S_r represents the idle distance of the robot until the stop signal is issued by the controller. The reaction time generally includes the response time of the safety-related equipment, the robot controller, motor drive, and communication latency. Furthermore, S_s is the braking distance of the robot until it stops completely, which is highly dependent on the braking performance of the robot, the present speed of the robot when the stop is issued, and the weight of the payload. In addition, C is an intrusion distance through which a part of the body (usually a hand) can move past the detected zone toward the hazard zone prior to actuation of the safety functions [31]. For instance, all possible intrusion of the human hands from the undetected zone should be considered if the robot system can only monitor a 2D plane. Based on consideration of the ISO standards, shifting from a 2D sensor to a 3D sensor can reduce the intrusion distance. When using a 2D laser scanner, a distance less than or equal to the 850-mm intrusion distance must be considered in the SSM function as C . Therefore, it is required to separate the human and the robot more than is necessary, which consequently limits the efficiency of the collaboration. On the other hand, when using a 3D sensor as the safety-related sensor, C can be neglected by only considering the measurement performance of the sensor.

Finally, Z_d and Z_r are the measurement uncertainties of the positions of the human and that of the robot. However, as some research shows, how to derive these parameters regarding uncertainties still remains not clear [11,18]. In this study, we follow the framework of IEC/TS 62,998 to use coverage interval as the measurement uncertainties. The coverage interval indicates the confidence level of the Gaussian distributed measurement error that meets the required safety integrity level [20]. In accordance with the required safety integrity level of $PL_r = d$, the measurement uncertainties are calculated as $Z_d = 5.16 \sigma$, where σ denotes the standard deviation of the measurement error.

Assuming that the robot decelerates with a constant braking performance a_s , (1) can be rewritten as follows:

$$S_p(t_0) = v_h(t_0)(T_r + T_s) + v_r(t_0)T_r + \frac{v_r(t_0)^2}{a_s} + C + Z_d + Z_r \quad (2)$$

where T_r is the reaction time of the robot system; and T_s is the time elapsed from the issuing of the stop signal until the robot stops completely. In addition, v_r and v_s represent the relative speed in the manner that it decreases the closest distance the most. Finally, the robot that violates the PSD should execute the protective stop function as follows [32]:

$$S_p(t_0) \leq S(t_0). \quad (3)$$

2.2. Potential runaway motion volume in task space

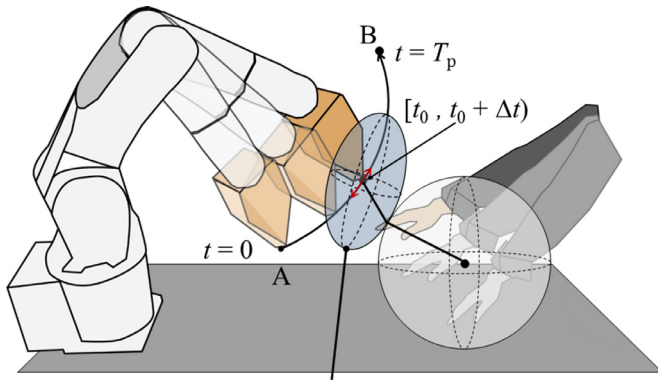
Despite this effort, the safety distance between the robot and the human may be insufficient with the presented PSD alone. For instance, popular permanent magnet servomotors, which are used to produce the driving force to move the joints of industrial robots, can generate faults for electrical, mechanical, and other external reasons [33,34]. It should be also noted that even though ISO/TS 15,066 requires to consider the acceleration capability of the robot, few studies have attempted to include the runaway motion of the robot [6].

In this study, PRAM-t is used to estimate the worst-case acceleration volume that the robot can move during the state of the runaway, as shown in Fig. 2 [29]. In the case where a robot makes a fault at time t_0 , it can be interpreted that the end-effector of the robot moves along a different path from that of the original one that has been planned in normal operation. For industrial robots that are designed for the manufacturing sites, it is required to have the capability of detection or tolerance to a single fault [5]. Therefore, it can be assumed that these robots have the capability to execute the protective stop function after a certain period of time, i.e., the reaction time or the communication time. Especially, in general, the motor apparatus also have independently capable of self-diagnosis function in case of failure. In this study, we assume the reaction time of an activation of a protective safety function is equivalent to the maximum reaction time of the motor drive.

Suppose $\mathbf{r} = (r_1, r_2, \dots, r_m)^T \in \mathbb{R}^m$ is a set of vectors that represents the position and orientation of the end-effector defined from a reference coordinate system fixed to the robot system, and $\mathbf{q} = (q_1, q_2, \dots, q_n)^T \in \mathbb{R}^n$ is the joint angle vector. The first-order relationship between two vectors, \mathbf{q} and \mathbf{r} , can be written as follows:

$$\mathbf{r} = \mathbf{f}(\mathbf{q}). \quad (4)$$

Further, velocity of the end-effector $\mathbf{v} \in \mathbb{R}$ can be expressed as



Potential RunAway Motion volume in task space

Fig. 2. Illustration of protective separation distance considering potential runaway motion in task space ellipsoid $RS_p(t_0)$ during $[t_0, t_0 + \Delta t]$. The typical case where an industrial manipulator is operated along a preliminary taught trajectory from A to B is considered and is calculated along the Mahalanobis distance.

$$\mathbf{v}(\mathbf{q}) = \mathbf{J}(\mathbf{q})\dot{\mathbf{q}} \quad (5)$$

where \mathbf{J} is the Jacobian matrix (\mathbf{J}) and $\dot{\mathbf{q}} = d\mathbf{q}/dt$.

Let $\mathbf{M}(\mathbf{q})$ is the inertia matrix; the acceleration of the robot end-effector can be computed as follows:

$$\ddot{\mathbf{v}}(\mathbf{q}) = \mathbf{J}(\mathbf{q})\tilde{\mathbf{M}}^{-1}(\mathbf{q})\tilde{\boldsymbol{\tau}}(\mathbf{q}) \quad (6)$$

where $\tilde{\boldsymbol{\tau}}$ is the normalized control force of joints

$$\tilde{\boldsymbol{\tau}} = [\tilde{\tau}_1, \tilde{\tau}_2, \dots, \tilde{\tau}_n], \quad \tilde{\tau}_i = \tau_i/\tau_{i\max}, \quad (7)$$

and $\tilde{\mathbf{M}}$ denotes the normalized \mathbf{M} :

$$\tilde{\mathbf{M}} = \mathbf{T}_\tau \mathbf{M}, \quad \mathbf{T}_\tau = \text{diag}\left(\frac{1}{\tau_{1\max}}, \frac{1}{\tau_{2\max}}, \dots, \frac{1}{\tau_{m\max}}\right). \quad (8)$$

Hence, all the sets of acceleration of the end-effector that can be obtained using the joint driving force become ellipsoids in the m-dimensional Euclidean space (i.e., DME) [35]. The main axis of the ellipsoid $\sigma_{d1}u_{d1}, \sigma_{d2}u_{d2}, \dots, \sigma_{dm}u_{dm}$ can be determined by calculating the singular value decomposition of $(\mathbf{J}\tilde{\mathbf{M}}^{-1})$:

$$\mathbf{J}(\mathbf{q})\tilde{\mathbf{M}}^{-1}(\mathbf{q}) = \mathbf{U}_d \boldsymbol{\Sigma}_d \mathbf{V}_d^T. \quad (9)$$

In accordance with (9), PRAM-t when the robot runs at time t_0 can be calculated under the assumption that the robot will follow the acceleration calculated by the DME during the reaction time of internal motor drive T_{ro} .

Finally, the PSD considering the PRAM-t RS_p is expressed by the following conditional equation that is dependent on the speed of the robot during the reaction equation that is dependent on the speed of the robot during the reaction time of the motor drive T_{ro} , which is shown in Fig. 3. What is to note is the PRAM-t is generally represented as an ellipsoid, and the acceleration value is dependent on the relative distance and direction between the robot and the human. Therefore, as shown in Fig. 2, the RS_p is calculated on the Mahalanobis distance considering the geometrical relationship between the ellipsoid and the sphere of the human body part distance.

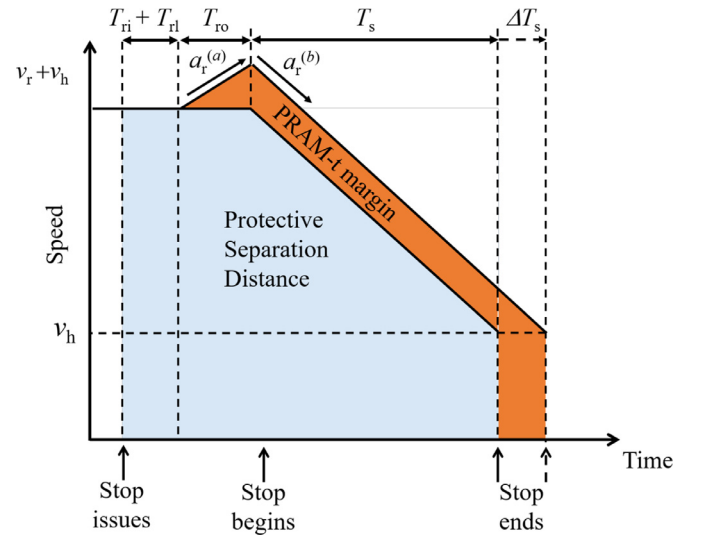


Fig. 3. Illustration of protective separation distance (blue colored area) and potential runaway motion in task space (orange-colored area), where v_h and v_r denote the relative speed of the operator and the robot, respectively, defined according to the closest distance plane; T_{r1} , T_{rl} , and T_{ro} denote the reaction time of the protective equipment, logical control device, and motor drive respectively. T_s , and ΔT_s represent the stopping time to make the speed of the robot zero and an increase in the stopping time due to the acceleration of the robot system respectively. Finally, $a_r^{(a)}$ and $a_r^{(b)}$ denote acceleration and deceleration performance of the robot, respectively. (For interpretation of the references to colour in this figure legend, the reader is referred to the web version of this article.)

$$RS_p(t_0) = S_p(t_0) + \frac{a_r^{(a)}T_{ro}^2 + a_r^{(b)}\Delta T_s^2}{2} + (v_h + v_r)\Delta T_s \quad (10)$$

where $a_r^{(a)}$ and $a_r^{(b)}$ represent acceleration calculated by the DME, and deceleration originating from braking performance of the robot, respectively. It should be noted that T_{rb} , T_{rl} , and T_{ro} denote the reaction time of the protective equipment, logical control device, and motor drive respectively. In addition, ΔT_s represents an increase in the stopping time due to the acceleration of the robot system. Consequently, RS_p should meet the following condition in addition to (3):

$$S_p(t_0) \leq RS_p(t_0) \leq S(t_0). \quad (11)$$

2.3. Maximum speed control and energy transfer during contact

The SSM method is a protective feature for securing PSD between the operator and the robot. In general, risk of contact can be defined as a combination of the probability of occurrence of harm and the severity of that harm [3]. In this respect, it should be noted that minor contact can be accepted for the case where the risk of contact between the human and the robot is negligible. In other words, the robot may maintain its tasks when the PSD is violated as far as the severity of the contact risk is acceptable. However, little guidelines or agreements have been made regarding the severity of the risk of contact, which is to be defined in terms of the probabilistic regulation. In this study, the permissible velocity limit is discussed based on the expected transfer energy using the biomechanical limits in ISO/TS 15066.

The kinetic energy matrix associated with the operational space $\Lambda(\mathbf{q})$ for non-redundant robots can be calculated by [36,37]

$$\Lambda(\mathbf{q}) = (\mathbf{J}(\mathbf{q})\mathbf{M}^{-1}\mathbf{J}^T(\mathbf{q}))^{-1}. \quad (12)$$

Further, (12) can be decomposed into

$$\Lambda^{-1} = \begin{bmatrix} \Lambda_v^{-1}(\mathbf{q}) & \bar{\Lambda}_{vw}(\mathbf{q}) \\ \bar{\Lambda}_{wv}^T(\mathbf{q}) & \Lambda_w^{-1}(\mathbf{q}) \end{bmatrix}. \quad (13)$$

Thus, a scalar value of the effective mass of the end-effector can be expressed as follows:

$$m_u = [\mathbf{u}^T \Lambda_v^{-1}(\mathbf{q}) \mathbf{u}]^{-1}, \quad (14)$$

and

$$i_u = [\mathbf{u}^T \Lambda_w^{-1}(\mathbf{q}) \mathbf{u}]^{-1}, \quad (15)$$

where m_u is the reflected robot inertia; and i_u is the reflected rotational robot inertia toward the \mathbf{u} direction. In this study, only m_u is treated as the effective mass of the end-effector of the robot due to the difficulty of estimating i_u in practice, and most of the trajectories performed by the robot in the experiment were translational movements. Finally, considering the dynamic contact between the human and the robot, expected transfer energy E when a simple two-body model is used can be written as follows:

$$E = \frac{1}{2} \mu v_{rel}^2 \quad (16)$$

$$\mu^{-1} = m_r^{-1} + m_h^{-1} \quad (17)$$

where μ is the reduced mass of the human and the robot; v_{rel} is the relative speed between the human and the robot; m_h represents the effective mass of the human; and m_r denotes the effective mass of the robot in the \mathbf{u} direction.

3. Experimental design

The purpose of experiments presented in this section is firstly to compare the separation distances between when using the 2D and 3D sensor as a safety-related sensor. For the comparison, battery assembly scenarios between the human and the robot were carried out. Second is



Fig. 4. Battery assembly task: Human-robot collaboration scenario used in the experiment. An example of the robot is equipped with a radio wave sensor system using a speed and separation monitoring function.

to investigate the effect of the potential acceleration of the robot in case of runaway by using actual information of the human and the robot. Two different orientations were demonstrated in the experiment because the effect of the potential runaway motion of the robot differs according to the posture of the robot and the relative distance vector between the human and the robot. The third is to investigate expected transferred energy assuming potential contact based on the dynamic properties of the robot and the biomechanical limit of human injury. Assuming foreseeable misuse of the human side, the simulation was carried out by using the instant velocity of the human and the robot. Our experiments were performed with the permission of the institutional review board of Nagoya University (approval no. 18-16).

3.1. HRC scenarios

Fig. 4 illustrates the battery assembly task performed by the participants and the robot system. Also, the task process of battery assembly task scenario for conducting the collaboration between the robot is summarized in Table 1. In the experiment, a six-axis robot arm (VS-060, Denso Wave, Japan) and a compressed air dispenser were used for applying the adhesive material. Experimental tools and layout of the human side are explained in Fig. 5. The robot performs the repetitive and simple task of applying the adhesive to the battery case, and the human operator performs a quality inspection and inserts the battery cell into the battery case after the task by the robot is completed. Two subjects who participated in the experiment were experts who were engaged for many years in the production line. The experiment was conducted until the operator completed four batteries after several trials of assembling the test batteries. A motion capture system (Venus 3D) was used to measure the relative distance between the three-dimensional position of the operator, and the end-effector of the robot. In this study, human hand contact between the robot was considered as the most hazardous event since the preliminary taught motion of the robot is demonstrated only around the working table. Therefore, the position of the participant's hands was measured, and the position of the chest was additionally measured as the central position of the participant. In case of emergency, the emergency stop button is located near the human work area and the experiment manager.

3.2. Protective equipment and test scenarios

Fig. 6 shows a block diagram of the control structure using two different types of sensors. Both the laser scanner (SE2L-H05P, IDEC,

Table 1
Summary of battery assembly task scenario process .

Type of task (Subject of action)	Process/ content	Classification
H1 - Bottom case task (Human)	Bottom case procurement	Moving
	Bottom case set	Operation
	Tag seal	Inspection
R1 - Bottom case adhesive injection (Robot)	Robot activation	Operation
	Adhesive injection	Injection
H2 - Upper case task (Human)	Upper case procurement	Moving
	Upper case set	Operation
	Bottom case collection	Moving
R2 - Upper case adhesive injection (Robot)	Robot activation	Operation
	Adhesive injection	Injection
H3 - Battery cell assembly task (Human)	Battery procurement	Moving
	Quality check1: electrical interference	Inspection
	Screwing1: middle case	Screwing
	Quality check2: position check	Inspection
	Bottom case procurement	Moving
	Tag seal	Operation
H4 - Switching task (Human)	Bottom case set	Operation
	Upper case insertion	Operation
	Screwing2: bottom case	Screwing
	Quality check3: final test	Inspection
	Transportation of assembled battery	Moving

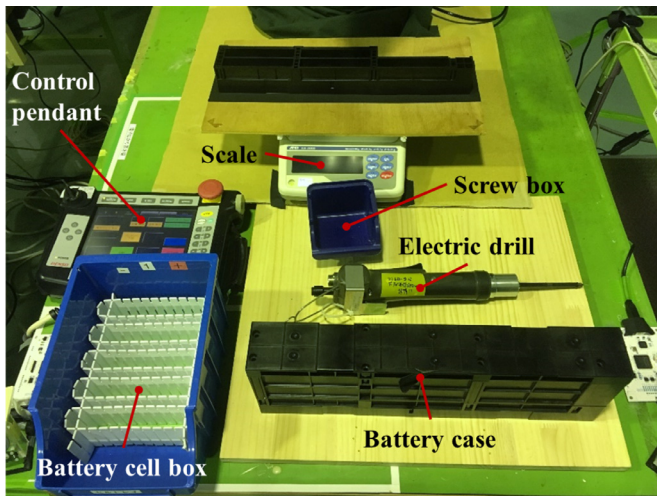


Fig. 5. Experimental layout and tools required for battery assembly task. The battery is complete when it is fixed to the battery cell with adhesive and screwed tightly.

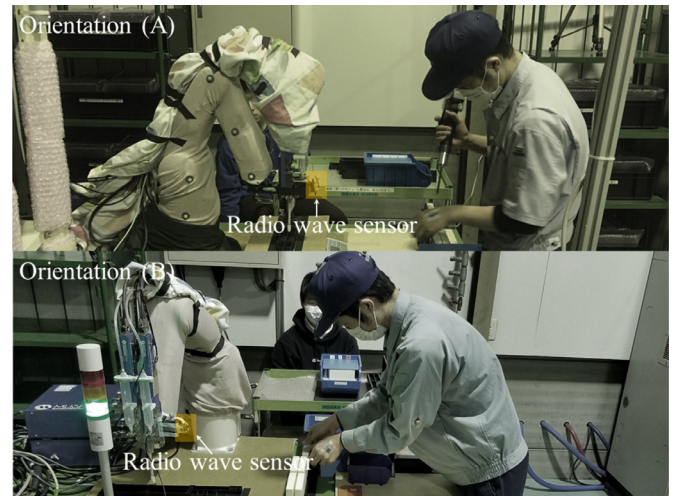


Fig. 7. Two different orientations of the robot. Orientation A demonstrates frontal interaction concept. Orientation B demonstrates perpendicular interaction concept.

Japan) and radio wave sensor system (SC1211AU2, Socionext, Japan) which uses frequency modulated continuous wave method is used to compute the safety distance; the speed of the robot is modified by external controllers. Accordance with the calculated safety distances, the speed of the robot is rescaled until it does not violate each safety distance. Fig. 7 shows two different concepts depending on relative postures between the robot and the human. PRAM-t was compared according to the relative orientation between the human and the robot, different postures of the robot were demonstrated. Relevant safety distances were computed based on physical parameters which are given by the robot manufacturer. Especially, the reaction time of the logical control device T_{rt} , and the motor drive T_{ro} was set as 100 ms, and 50 ms respectively. Details of different test cases with relevance to protective equipment have been defined in the following.

3.2.1. Test case 1: layout using the laser scanner

Fig. 8 shows the layout of the presented Test Case 1 scenario. Safety distance between the robot and the human was calculated based on the minimum distance criterion with sensor latency T_{rt} of 40 ms [31]. Body parts such as a human hand cannot be continuously detected when using the 2D laser scanner to monitor the movement of the operator. Therefore, it is required to take into account an appropriate margin distance according to the installed position of the laser scanner [31]. Accordance with the height of the Laser scanner (0.9 m), C was chosen as 0.85 m. The safety distance between the operator and the robot was calculated from the position of the maximum reach of the robot. The

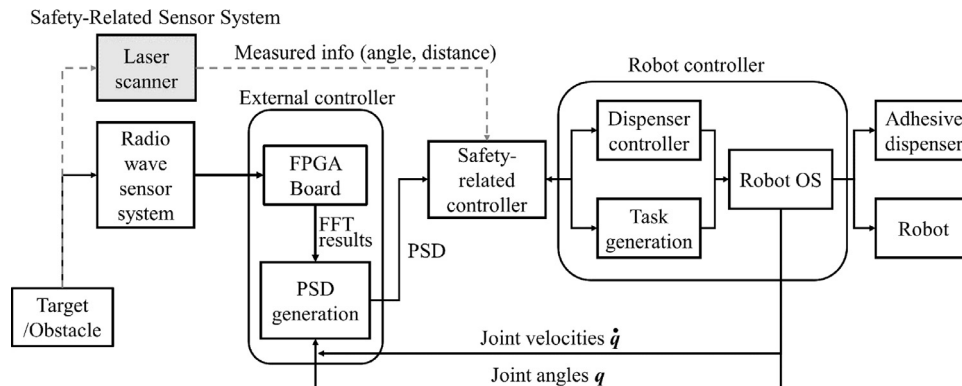


Fig. 6. Block diagram of experimental hardware and software setup dependent on the safety-related sensors. The speed of the robot is modified according to the relative distance and velocity between the human and the robot.

experiments were conducted according to the orientations of A and B of the robot.

3.2.2. Test case 2: layout using the radio wave sensor system

Fig. 9 shows the layout of the Test Case 2 scenario when using the radio wave sensor system. A total of three radio sensors S1, S2, and S3 were installed on the end-effector and both ends of the workspace. The specific parameters of the radio wave sensors were configured based on their displacements and receptivities. All carrier frequency of the radio wave sensors were set as 24.14 GHz, and sweep frequencies were set as 180 MHz. Closest distance and its velocity was calculated based on the FM-CW method with FFT size of 2048, and the Hamming window was used for its digital signal processing. In order to avoid radio wave interferences and ghost targets, different sweep sampling time 1024 us, 614 us, and 409 us were used for S1, S2, and S3 respectively. Both radio wave sensors placed on the end of the table was used to confirm whether the participant is in the workspace. The radio wave sensor placed on the end effector S1 is enabled only when the table placed S2, or S3 gives distance less than 1 m with latency T_{ri} of 30 ms. The PSD was calculated based on the distance between the end-effector and the closest body parts of the operator taken by the S1. Intrusion distance C was ignored in the PSD calculation because the relative distance between the body part of the human and the robot can be observed. The measurement uncertainty Z_d was set as 16 cm considering the measurement error of the used radio wave sensor follows the Gaussian distribution having 3 cm of standard deviation, and coverage interval of $PL_r = d$ requires 5.16σ [20,21]. In the same way as in Test Case 1, experiments were conducted for the orientations of A and B of the robot.

3.3. Evaluation metric

3.3.1. Productivity metric

In each trial, the protective equipment has been varied, which were presumed to have an impact on separation distance and cycle time mainly due to the decreased intrusion distance. The productivity of the HRC application for the presented test scenarios when using different protective equipment was evaluated by the workspace occupancy and the application time. With respect to the HRC analytical models for productivity in the workspace, the following shop floor space (FS) is and an average separation distance was used for the evaluation [22]:

$$FS = (x_i^{\max} - x_i^{\min}) \times (y_i^{\max} - y_i^{\min}), \quad (18)$$

where x_i^{\max} and y_i^{\max} are the maximum values of the x and y positions, respectively, for the resources, including the operator and the robot; and x_i^{\min} and y_i^{\min} are the minimum values of the x and y positions during the i th task, respectively. Each x and y is defined in accordance with the layout of the workspace. In addition, the application cycle time required to complete the task T_H is assessed as an additional metric:

$$T_H = \sum_{i=1}^n T_c^i, \quad (19)$$

where T_c^i is the time consumed during the i th task; and n represents the task number conducted by the operator.

3.3.2. PRAM-T simulation analysis

The main goal of the analysis is to find a distinction between the presented orientations. Since the radio wave sensor used in this study is

the SISO sensor which allows measuring only the relative distance and velocity, simulation based on measured samples by motion capture system was used to investigate the effect of the runaway motion of the robot. It is presumed that the runaway acceleration of the robot will differ against each orientations A and B due to the PRAM-t is represented as an ellipsoid. For the same reason, the acceleration of the robot's runaway motion is dependent on the relative distance and direction between the robot and the human. Therefore, the runaway acceleration of the robot can differ according to the relative position of the human body parts. With respect to the effect of the runaway motion of the robot into the PSD, a comparison of runaway margin $RS_p - S_p$ is used for the evaluation for each body part.

In addition, the result is normalized with torque and arm length value since the effect of PRAM-t can differ according to the performance of the robot used in the experiment. However, due to the computation payload and calculation resources, only one cycle time period of the sample from participants was used for the normalization.

3.3.3. Velocity boundaries and transfer energy analysis

The purpose of the simulation is to investigate the expected transfer energy to calculate the permissible velocity limit. For the case of using properly designed SSM, no collision can occur except for intentional or misuse by the human because of the nature of the non-contact oriented collaborative system. While the SSM implementation allows avoiding foreseeable contact, some of the contact during the application may be conditionally acceptable if the risk of the contact is minor. From this insight, this simulation includes the approach of estimating the expected transfer energy of potential contact in the current dynamic state. First, the contact scenario is established using the reduced-mass two-body model and the effective mass of the robot end-effector derived by the mechanical properties of the robot. After the contact scenario is modeled, the threshold of the robot speed is identified based on the biomechanical limit where the human feels pain. The mass of the human hand is assumed to be fixed at 0.6 kg, and the biomechanical energy limit of the human hand was set at 0.49 J according to the ISO/TS 15,066 [6]. Referring to (14), we recall that the effective mass of the robot differs according to the relative position of the human and the robot. Therefore, the expected transfer energy was computed between each part of the human body during the presented experiment.

4. Results

In this section, the cycle times achieved with the different types of sensors and orientation in each of the test cases as defined in Section 3.3.1 are presented in the following. In addition, PRAM-t simulation and velocity boundary analysis were conducted based on the obtained motion capture data samples as shown in Section 3.3.2, and 3.3.3.

4.1. Comparison of cycle times

Table 2 lists the total cycle time, average and maximum velocity of the robot for each task when the application is held without any intrusion from the human operator. The comparison results of the mean cycle times from the experiment are summarized in Fig. 10. In comparison to when using the laser scanner, the mean cycle time of the moving task was reduced from 17.5 s to 4.6 s and from 13.1 s to 4.7 s for orientations A and B respectively in case of using the radio wave

Table 2

Robot cycle time, average and maximum velocity for each tasks without intrusion .

Type of task (Robot)	Cycle time(s)	Average velocity \bar{v}_r (mm/s)	Maximum velocity $\max(v_r)$ (mm/s)
R-1 Bottom case adhesive injection	45.9	88	509
R-2 Upper case adhesive injection	50.6	94	452

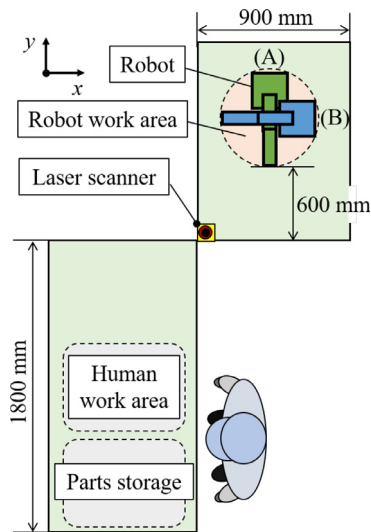


Fig. 8. Test Case 1: Layout when using the 2D laser scanner as the safety-related sensor. A layout was chosen to minimize moving path and risk of falls of the operator based on the risk assessment. Two different orientations of the robot, A and B, were tested.

sensor. In addition, the total mean cycle time had no much difference according to the orientations in the case of using the laser scanner. When using the radio wave sensor, the total mean cycle time of orientation A was shorter than that of B. In particular, radio B had the longest mean cycle time for waiting of 35.1 s. As a result, the mean cycle time was shortened when the orientation of the robot was A, and the mean cycle time increased when the orientation was B.

4.2. Comparison of floor space

Fig. 11 and Fig. 12 shows the heat map of the end-effector of the robot and the two participants during the task scenario of orientation A when using a laser scanner and radio wave sensor respectively (orientation B was similar to that of A and had no much difference). When using the radio wave sensor, compared with the laser scanner, the shop floor space and average separation distance both decreased. Table 3 summarizes a comparison of the shop floor space required for each operation in the experiment and the mean values of the separation distances between the closest human body parts. When using the radio

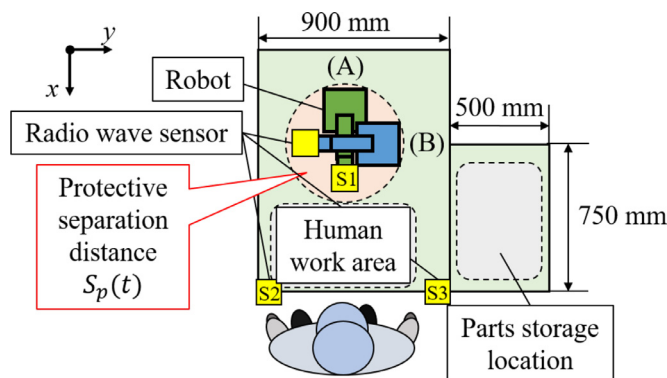


Fig. 9. Test Case 2: Layout when using the 3D radio wave sensor system as the safety-related sensor. Three radio wave sensors S1, S2, and S3 were installed on the end-effector of the robot, and each side end of the work area respectively. First, when the two sensors in the side end detect the human body, the radio wave sensor system is enabled. Second, only the radio wave sensor installed on the end-effector of the robot detects the human hand and slows or stops the robot according to the calculated protective separation distance. Finally, two different orientations, A and B, were tested.

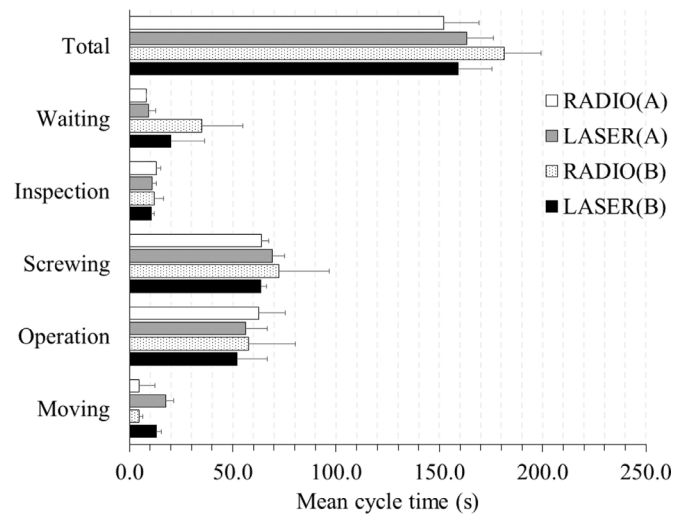


Fig. 10. Comparison of mean cycle time according to type of battery assembly work. Waiting indicates the waiting time of the operator for the robot to finish its task. The operation time includes battery assembly, attachment of the serial number seal, and manipulation of the robot. The moving time includes activities of transportation of materials.

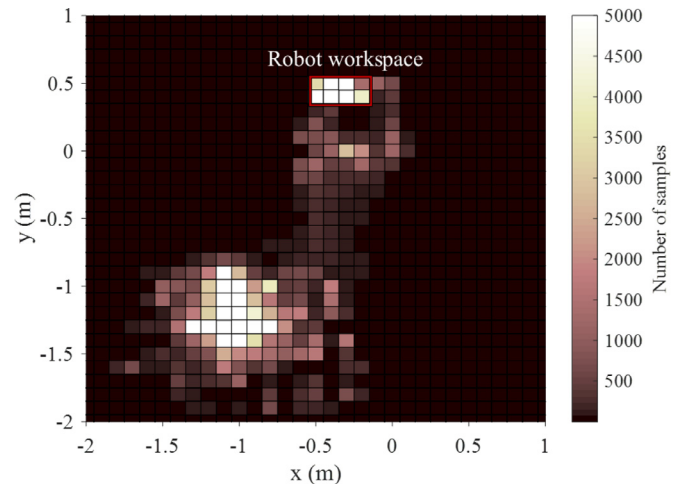


Fig. 11. Heat map of the end-effector and the two participants including chest and both hands during the task scenario of orientation A for laser scanner layout. Each mesh grid represents 1cm² in accordance to the coordinates shown in Fig. 8.

wave sensor, compared with the laser scanner, the shop floor space FS decreased by 58% and 20% for the orientation A and B respectively. Also, when using the radio wave sensor, in comparison with the laser scanner, the average separation distance decreased by 50% and 40% for the orientation A and B respectively.

4.3. Frequency of intrusion

Fig. 13 shows the data compiled for participant 1 in orientation A, comparing the $S_p(t)$ and the actual separation distance $S(t)$ from the participant's chest to the robot end-effector when using a laser scanner as the safety-related sensor. Fig. 14 shows data compiled for participant 1 in orientation B, comparing the $S_p(t)$ and the actual separation distance $S(t)$ from the participant's left hand when using a radio wave sensor system as the safety-related sensor. Both Fig. 13, and Fig. 14 are shown in duration time of 300 s to include one cycle for finishing the battery assembly task among the four total battery completion. As shown in Fig. 13, intrusions were observed during the moving task

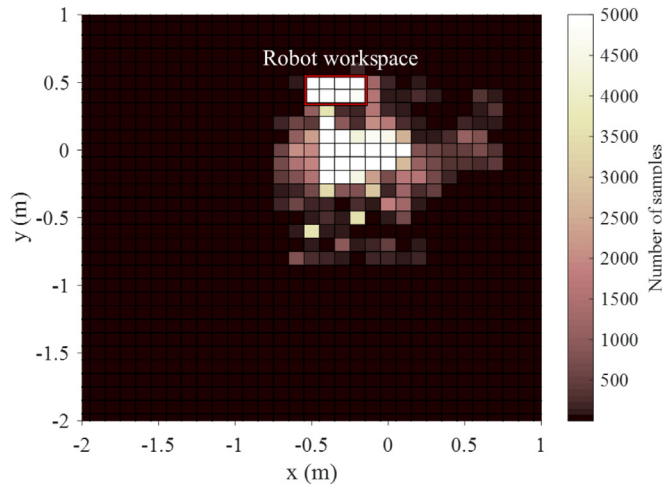


Fig. 12. Heat map of the end-effector and the two participants including chest and both hands during the task scenario of orientation A for radio wave sensor layout. Each mesh grid represents 1cm^2 in accordance to the coordinates shown in Fig. 9.

Table 3

Results of the required floor space (*FS*) and comparison of the average separation distance (*S*) between the end-effector and the body parts of the operator .

	Laser (A)	Radio (A)	Laser (B)	Radio (B)
<i>FS</i> (m^2)	4.77	2.01	4.40	3.49
<i>S</i> (m)	1.58	0.79	1.76	0.69

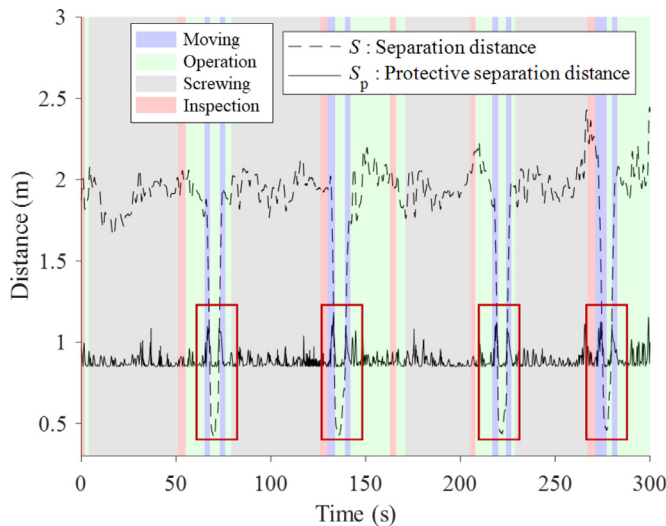


Fig. 13. Comparison of the protective separation distance S_p and the separation distance S between the chest part of the subject and the end-effector of the robot (orientation A) when using a laser scanner. Red rectangles show intrusion by the human operator during the moving task.

when using the laser scanner for orientation A and was same with that of the orientation B. Also, intrusion was observed only during the moving task in case of using radio wave sensor for the orientation A. In case of using radio wave sensor for orientation B, intrusions were observed during screwing and inspection task (Fig. 14). As a result, in case of using the radio wave sensor for orientation B, robot halted 41 times (27 times and 14 times for participant 1 and 2 respectively) for the screwing task of the human operator.

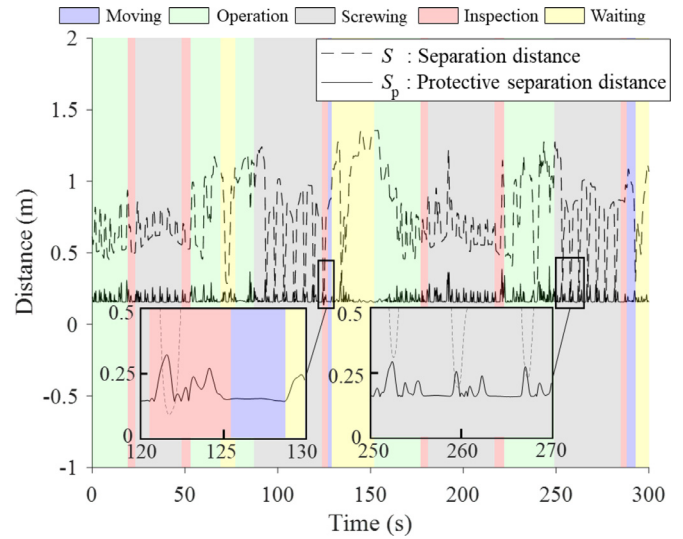


Fig. 14. Comparison of the protective separation distance S_p and the separation distance S between the left hand of the subject and the end-effector of the robot (orientation B) when using a radio wave sensor. Some epoch is highlighted to show intrusion by the human operator during the screwing, and inspection task.

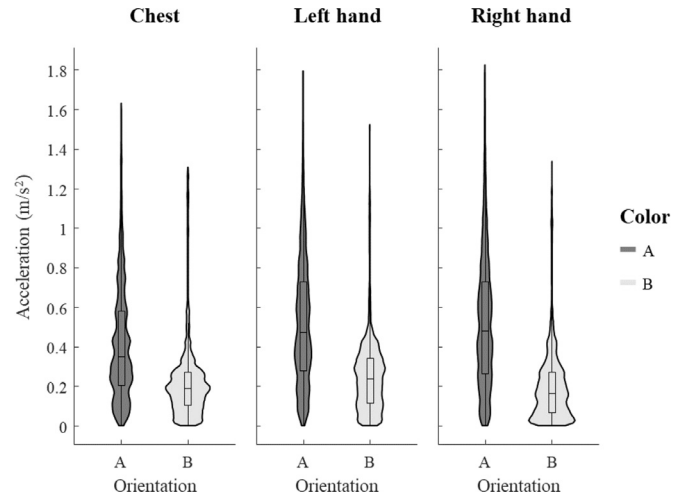


Fig. 15. Acceleration calculated by DME to each body part of the participants according to the relative orientation between the human and the robot when using a radio wave sensor as the safety-related sensor.

4.4. Comparison of protective separation distance and PRAM-t

For comparison of PRAM-t, runaway acceleration of the robot respect to the relative position of the human and the robot was computed based on experimental setup shown in Section 3.2. Fig. 15 shows a comparison of acceleration calculated by DME ellipsoid using measured position data of subjects and the robot end-effector (123687 samples total). As a result, the mean runaway acceleration of the robot decreased by changing the orientation from A to B for the chest (45%), left hand (61%), and right hand (51%).

Fig. 16 shows a comparison of runaway margin $RS_p - S_p$ with respect to each body part of the participants when using the radio wave sensor. Regarding the results, the mean runaway margin decreased by 31%, 61%, and 60% for the chest, left hand, and right hand, respectively. In addition, all the maximum values of the runaway margin during the experiment were less than 6 cm.

Finally, the simulation result was normalized by scaling the length of the robot arm and the maximum joint torque of the robot is shown in Fig. 17. The simulation assumes that all the arm lengths and the

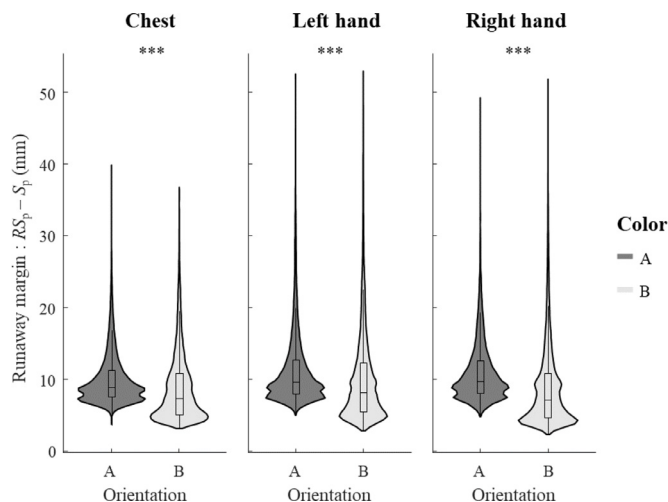


Fig. 16. Runaway margin $RS_p - S_p$ of each body part of the participants according to the relative orientation between the human and the robot when using a radio wave sensor as the safety-related sensor.

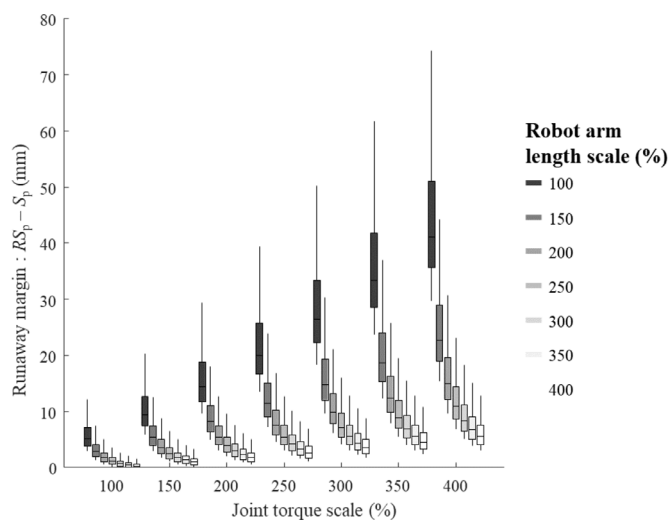


Fig. 17. Simulation result using one cycle sample of the battery assembling task conducted by one of the participants in the layout of orientation A. Robot arm length and the maximum joint torque were scaled based on the physical parameters of VS-060.

maximum joint torques are increased with the same proportion for the robots used in the experiment. Further, the results were summarized to include all the runaway margin respect to the specific body parts of the subjects during one cycle application of the experiment. From the results, as the length of the robot’s arm increased, the mean runaway margin also increased. For example, when only the maximum torque was varied, the mean runaway margin 2.7 times, and 7.5 times increased when the maximum joint torque increased 2 times, and 4 times respectively. On the other hand, as the length of the robot arm increased, the trend tends to decrease. For instance, when only the length of the robot arm was varied, the mean runaway margin decreased to 37% and 14% when the length scale of the robot arm increased 2 times and 4 times respectively.

4.5. Velocity boundaries and transfer energy analysis based on dynamic properties of the robot

In order to derive maximum permissible velocity, transfer energy was computed in accordance with the experimental setup shown in Section 3.3.3. Fig. 18 shows an example of the velocity boundaries of

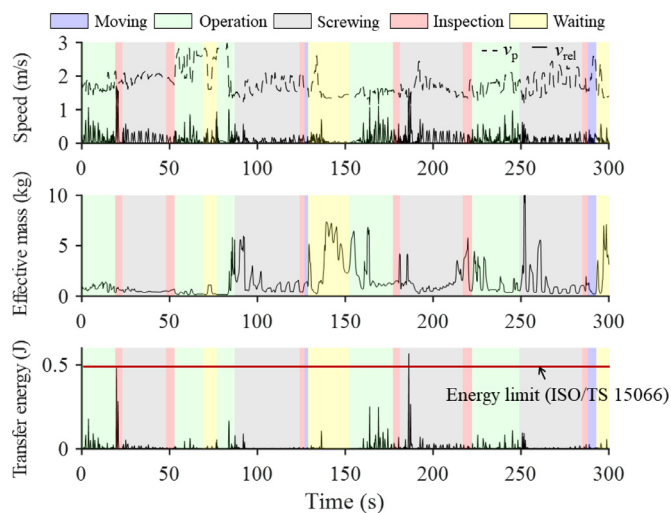


Fig. 18. Velocity boundary of the robot end-effector and expected transfer energy to the subject when using the radio wave sensor as the safety-related sensor for orientation A, where v_{rel} is the relative speed between the end-effector and the human right hand, and v_p is the permissible velocity limit calculated based on dynamic properties of the robot.

the robot end-effector and the expected transfer energy calculated by relative speed and effective mass between the participant and the robot when using the radio wave sensor as a safety-related sensor for orientation A. From the result, it can be known that transfer energy and relative speed were high enough to violate the energy limitation and maximum permissible velocity during the screwing task (180 s).

5. Discussion

5.1. Cycle time and frequency of intrusion

Contrary to what we expected, it can be known that the orientation B requires more cycle time than that of the A as shown in Fig. 10. The major reason for this is considered as due to the increased waiting time for the operator until the robot finishes its task. One of the reasons that the waiting time has been increased compared to that of orientation A can be explained by the intrusion of the participant into the PSD during the regular operation of the robot. Further, the screwing task of orientation B took 10 seconds longer on average than orientation A. According to the comment from the participants, they felt unsettled when the robot halts and it made their tasks were less productive until they completely moved away from the allowable safety distance.

The results from the orientation A group indicate that the cycle time when using the 3D sensor as a safety-related sensor can be decreased in terms of reducing the time cost for the moving task. However, the result of the orientation B group shows that the cycle time can rather increase with frequent access to the PSD. It can be interpreted as more attention should be given to an estimation of potential intrusion in the process designing stage. Therefore, it is important to configure and utilize the appropriate layout even if the separation distance between the human and the robot is shortened because of the 3D sensor.

5.2. Comparison of floor space and potential contact scenarios

The result of Table 3 shows the shop floor space benefits when shifting from a 2D sensor to a 3D sensor. First, it can be known that FS is largely reduced when using the radio wave sensor for both orientations A and B compared to that of the laser scanner from Table 3. The main reason for the FS is decreased is mainly due to the configuration of the intrusion distance is diminished when using the radio wave sensor. Conversely, when using the radio wave sensor, the FS of orientation B

decreased less than that of orientation A. Considering that the decrease of the mean separation distance of both orientations A and B were similar, this is thought to be due to the difference of the moving range of the operator caused by the difference of the layout, such as the direction of the battery displacement.

While 3D sensors allow higher efficiency, it is important to secure the operator safe taking into account potential contact scenarios. Due to the conventional 2D sensors force the HRC system to consider additional intrusion distance into the PSD, the probability of contact between the robot and the human due to the malfunction of the robot has little been discussed. However, the comparison of *FS* shows that the workspace sharing HRC task may result in physical contact since the separation distance between the human and the robot has been decreased below the length of the human arm (850 mm). Considering the range of the human arm motion and that of the robot when using the 3D sensors, the risk of physical contact may not be ignored during the malfunctioning state of the robot or the foreseeable misuse of the human side.

Another to be mentioned is that *FS* only evaluates only the movement of the operator's body. In practice, required shop floor space comprises space occupancy of the robot as well as the human operator. In the present study, the shop floor space of the end-effector of the robot was $0.09m^2$, which is expected that other applications will show difference (Fig. 12). Thus, in a strict manner, a proper evaluation of shop floor space should include the whole movement of the robot arm during the task scenario.

5.3. PRAM-T and effect of relative human and robot orientation

As shown in Fig. 16, the mean runaway margin $RS_p - S_p$ of orientation B was smaller than that of A for all of the measured body parts. The set of runaway accelerations of most commercially available vertical articulated robots, including the VS-060 used in this experiment, can be expressed as an ellipsoid through the DME, and the main axis tends to be formed in the frontal direction of the robot. In the same context, the reason why the volume of PRAM-t for the case of orientation A was larger than that of B was that orientation A was more affected by the frontal main axis of the acceleration ellipsoid than B. In the experiment, although the increment of the PSD due to PRAM-t was estimated to be smaller than 6 cm, it may increase depending on the acceleration/deceleration performance of the robot, the reaction time of the robot, and the traveling speed of the robot. Especially, from the result of Fig. 17, it can be known that the acceleration of the robot in the runaway state is proportional to the power of the motor. On the other hand, acceleration in the runaway state had a negative relationship with the increase of the robot arm length which can be explained by increasing the length of the arm can make the inertia matrix bigger. However, considering the mass of the robot arm may also increase according to the length of the arm gets longer, changing the reach of the robot might affect more than the result shown in this study.

5.4. Relationship between transferred energy and robot speed when using speed and separation monitoring

In the case where the probability of collision is not ignorable but its severity of contact is acceptable, minor contact may also be conditionally acceptable in terms of risk assessment. For example, as shown in Fig. 18, it can be seen that only the calculated transfer energy around 180 s has a higher value than that of the suggested biomechanical limit. During the HRC scenario where the SSM and PFL are both implemented, the robot may not stop its task necessarily but strictly follow the permissible velocity limit derived by expected transfer energy even though the PSD is violated. It should be noted that the presented study includes limitations such as not considering the effect of the inertia of the effective mass which can make the expected transfer energy bigger especially during the high-speed control of the robot. Nevertheless, it is

thought that the proposed framework can link between SSM and PFL to design and control robots for a higher level of safety and productivity. In order to realize the fusion of plural safety functions in unstructured environments, practice insights are fundamental, such as on-robot sensing techniques and point of interest analysis of the robot end-effector.

6. Conclusion

In this study, two relative postures of the operator and the robot were examined to estimate potential runaway motion of the robot—frontal orientation (A), and perpendicular orientation (B). From the result, it was found that the volume of potential runaway motion space for the case of orientation A is larger than that of B because orientation A is more affected by the main axis of the acceleration ellipsoid than B. Therefore, in order to reduce the runaway distance, it is effective to avoid the frontal arrangement of robots and humans.

Considering the basic concept of risk, it is reasonable to take the severity of contact into the SSM function. In this respect, expected transferred energy was used to calculate the maximum permissible velocity of the robot assuming potential contact based on the dynamic properties of the robot and the biomechanical limit of human injury. The proposed framework is thought to be useful to link between SSM and PFL to design and control robots for a higher level of safety and productivity.

CRedit authorship contribution statement

Eugene Kim: Conceptualization, Methodology, Software, Resources, Data curation, Validation, Formal analysis, Writing - original draft, Writing - review & editing, Supervision, Investigation, Visualization. **Yoji Yamada:** Methodology, Supervision, Writing - review & editing, Project administration, Funding acquisition. **Shogo Okamoto:** Supervision, Visualization, Project administration, Writing - review & editing. **Mikihiro Sennin:** Software, Validation, Data curation, Formal analysis. **Hiroki Kito:** Software, Data curation.

Declaration of Competing Interest

The authors declare that they have no known competing financial interests or personal relationships that could have appeared to influence the work reported in this paper.

Acknowledgments

This study was conducted through the “Knowledge Hub Aichi” project (Stage II-R6), which is financially supported by the Aichi Science & Technology Foundation.

References

- [1] S. Robla-Gómez, V.M. Becerra, J.R. Llata, E. Gonzalez-Sarabia, C. Torre-Ferrero, J. Perez-Oria, Working together: a review on safe human-robot collaboration in industrial environments, *IEEE Access* 5 (2017) 26754–26773.
- [2] P.A. Lasota, T. Fong, J.A. Shah, et al., A survey of methods for safe human-robot interaction, *Foundations and Trends® in Robotics* 5 (4) (2017) 261–349.
- [3] Safety of machinery – General principles for design – Risk assessment and risk reduction, ISO 12100:2010.
- [4] A. Realyvásquez-Vargas, K.C. Arredondo-Soto, J.L. García-Alcaraz, B.Y. Márquez-Lobato, J. Cruz-García, Introduction and configuration of a collaborative robot in an assembly task as a means to decrease occupational risks and increase efficiency in a manufacturing company, *Robot Comput Integr Manuf* 57 (2019) 315–328.
- [5] Robots and robotic devices—Safety requirements for industrial robots—Part 1: Robots, ISO 10218-1:2011.
- [6] Robots and robotic devices—Collaborative robots, ISO/TS 15066:2015.
- [7] S. Szabo, W. Shackelford, R. Norcross, J. Marvel, A testbed for evaluation of speed and separation monitoring in a human robot collaborative environment, US Department of Commerce, National Institute of Standards and Technology, 2012.
- [8] J.A. Marvel, Performance metrics of speed and separation monitoring in shared workspaces, *IEEE Trans. Autom. Sci. Eng.* 10 (2) (2013) 405–414.

- [9] J.A. Marvel, R. Bostelman, A cross-domain survey of metrics for modelling and evaluating collisions, *Int. J. Adv. Rob. Syst.* 11 (9) (2014) 142.
- [10] J.A. Marvel, J. Falco, I. Marstio, Characterizing task-based human–robot collaboration safety in manufacturing, *IEEE Transactions on Systems, Man, and Cybernetics: Systems* 45 (2) (2014) 260–275.
- [11] J.A. Marvel, R. Norcross, Implementing speed and separation monitoring in collaborative robot workcells, *Robot Comput Integr Manuf* 44 (2017) 144–155.
- [12] B. Lacevic, P. Rocco, Kinetostatic danger field—a novel safety assessment for human-robot interaction, *Proceedings of the Intelligent Robots and Systems, 2010 IEEE/RSJ International Conference on*, IEEE, 2010, pp. 2169–2174.
- [13] B. Lacevic, P. Rocco, A.M. Zanchettin, Safety assessment and control of robotic manipulators using danger field, *IEEE Trans. Rob.* 29 (5) (2013) 1257–1270.
- [14] C. Byner, B. Matthias, H. Ding, Dynamic speed and separation monitoring for collaborative robot applications—concepts and performance, *Robot Comput Integr Manuf* 58 (2019) 239–252.
- [15] D. Kulić, E. Croft, Pre-collision safety strategies for human-robot interaction, *Auton Robots* 22 (2) (2007) 149–164.
- [16] T. Hattori, Y. Yamada, S. Mori, S. Okamoto, S. Hara, Psychological experiments on avoidance action characteristics for estimating avoidability of harm to eyes from robots, *Proceedings of the 2012 IEEE/RSJ International Conference on Intelligent Robots and Systems*, IEEE, 2012, pp. 5400–5405.
- [17] A.R. Sanderud, M. Niitsuma, T. Thomessen, A likelihood analysis for a risk analysis for safe human robot collaboration, *Proceedings of the Emerging Technologies & Factory Automation (ETFA)*, 2015 IEEE 20th Conference on, IEEE, 2015, pp. 1–6.
- [18] E. Kim, R. Kirschner, Y. Yamada, S. Okamoto, Estimating probability of human hand intrusion for speed and separation monitoring using interference theory, *Robot Comput Integr Manuf* 61 (2020) 101819.
- [19] B. Matthias, T. Reisinger, Example application of ISO/TS 15066 to a collaborative assembly scenario, *Proceedings of the ISR 2016: 47th International Symposium on Robotics*, Proceedings of, VDE, 2016, pp. 1–5.
- [20] **Safety of machinery - Electro-sensitive protective equipment - Safety-related sensors used for protection of person, IEC/TS 62998.**
- [21] E. Kim, Y. Yamada, S. Okamoto, Improvement of safety integrity level by multiplexing radio wave sensors, *Proceedings of the System Integration, 2017 IEEE/SICE International Symposium on*, IEEE, 2017, pp. 942–947.
- [22] P. Tsarouchi, G. Michalos, S. Makris, T. Athanasatos, K. Dimoulas, G. Chryssolouris, On a human–robot workplace design and task allocation system, *Int. J. Computer Integr. Manuf.* 30 (12) (2017) 1272–1279.
- [23] M. Zlatanski, P. Sommer, F. Zurfluh, G.L. Madonna, Radar sensor for fenceless machine guarding and collaborative robotics, *Proceedings of the 2018 IEEE International Conference on Intelligence and Safety for Robotics (ISR)*, IEEE, 2018, pp. 19–25.
- [24] S. Kumar, S. Arora, F. Sahin, Speed and separation monitoring using on-robot time-of-flight laser–ranging sensor arrays, *arXiv preprint arXiv:1904.07379* (2019).
- [25] H. Liu, L. Wang, Collision-free human-robot collaboration based on context awareness, *Robot Comput Integr Manuf* 67 (February 2021), <https://doi.org/10.1016/j.rcim.2020.101997>.
- [26] A. Sengupta, F. Jin, R. Zhang, S. Cao, mm-pose: real-time human skeletal posture estimation using mmwave radars and CNNs, *IEEE Sens J (Early Access)* (2020) 1–1, <https://doi.org/10.1109/JSEN.2020.2991741>.
- [27] A.M. Zanchettin, P. Rocco, S. Chiappa, R. Rossi, Towards an optimal avoidance strategy for collaborative robots, *Robot Comput Integr Manuf* 59 (2019) 47–55.
- [28] L. Ma, P. Bazzoli, P.M. Sammons, R.G. Landers, D.A. Bristow, Modeling and calibration of high-order joint-dependent kinematic errors for industrial robots, *Robot Comput Integr Manuf* 50 (2018) 153–167.
- [29] Y. Yamada, S. Takeda, T. Nishiyama, S. Okamoto, Potential runaway motion volume in task space for estimating the probability of occurrence of a human-robot collision, *Proceedings of the 2018 IEEE International Conference on Intelligence and Safety for Robotics (ISR)*, IEEE, 2018, pp. 34–39.
- [30] **Robots and robotic devices—Safety requirements for industrial robots—Part 2: Robot systems and integration, ISO 10218-2: 2011.**
- [31] **Safety of machinery – Positioning of safeguards with respect to the approach speeds of parts of the human body(2010), ISO 13855:2010.**
- [32] **Safety of machinery – Emergency stop function – Principles for design, ISO 13850.**
- [33] J. Halme, Condition monitoring of a material handling industrial robot, *Proceedings of the 19th International Congress Condition Monitoring and Diagnostic Engineering Management, COMADEM 2006*, Luleå University of Technology, 2006.
- [34] A.A. Jaber, R. Bicker, Industrial robot backlash fault diagnosis based on discrete wavelet transform and artificial neural network, *American Journal of Mechanical Engineering* 4 (1) (2016) 21–31.
- [35] T. Yoshikawa, Analysis and design of articulated robot arms from the viewpoint of dynamic manipulability, *Robotics Research: The 3rd International Symposium*, MIT Press, 1986, pp. 273–279.
- [36] O. Khatib, Inertial properties in robotic manipulation: an object-level framework, *Int J Rob Res* 14 (1) (1995) 19–36.
- [37] S. Haddadin, S. Haddadin, A. Khoury, T. Rokahr, S. Parusel, R. Burgkart, A. Bicchi, A. Albu-Schäffer, On making robots understand safety: embedding injury knowledge into control, *Int J Rob Res* 31 (13) (2012) 1578–1602.